photonics

MDPI

Article

Robust Demodulation Algorithm for Multimode Sapphire Fiber Bragg Grating High-Temperature Sensors Based on Analytic Envelope Extraction

Hongtian Zhu [1], Rui Liang [1], Qi Zhang [1], Enbo Wang [1], Zhaoyi Li [1], Zhichun Liu [1], Zhenyin Hai [1,*] and Chenyang Xue [1,2]

[1] School of Aerospace Engineering, Xiamen University, Xiamen 361102, China; 35020230156555@stu.xmu.edu.cn (H.Z.); liangrui@stu.xmu.edu.cn (R.L.); zhangqi@stu.xmu.edu.cn (Q.Z.); wangenbo@stu.xmu.edu.cn (E.W.); 34520241151592@stu.xmu.edu.cn (Z.L.); liuzhichun@xmu.edu.cn (Z.L.); xuechenyang@xmu.edu.cn (C.X.)

[2] The Key Laboratory of Instrumentation Science and Dynamic Measurement, Ministry of Education, North University of China, Taiyuan 030051, China

* Correspondence: haizhenyin@xmu.edu.cn

Abstract

Multimode sapphire fiber Bragg gratings (SFBGs) are essential for high-temperature monitoring in aerospace and energy sectors. However, their unclad structure inherently causes spectral broadening and severe modal asymmetry. Intense thermal blackbody radiation further degrades the signal-to-noise ratio at extreme temperatures. These combined factors render conventional single-peak demodulation methods highly unreliable. To resolve these challenges, this study proposes a three-stage demodulation framework tailored for multimode SFBG sensors. The process begins with an optimized 201-point moving-average filter. This filter suppresses detector shot noise and intermodal ripples while strictly preserving the steep cut-off edges of the spectrum. A Hilbert transform applied in the linear power domain then extracts the analytic envelope to adaptively isolate the dominant 3 dB reflection sub-band without relying on fixed intensity thresholds. A localized zero-centered parabolic fitting operator subsequently resolves the continuous resonant peak with picometer-level precision. We evaluated this framework through static and long-term isothermal sensing experiments from 23 °C to 1400 °C. The extracted Bragg wavelengths maintain a polynomial fitting correlation exceeding 0.9981 across the entire calibrated range. During 60 min continuous isothermal dwelling at 1000 °C, 1200 °C, and 1400 °C, the standard deviations of the measurements reached 0.186 nm, 0.098 nm, and 0.158 nm respectively. These stability metrics substantially outperform conventional centroid, direct maximum, and Gaussian fitting techniques. The proposed framework directly mitigates multimodal spectral distortion and thermal noise, offering a highly accurate and computationally efficient demodulation protocol for harsh-environment optical fiber sensing.

Keywords: sapphire fiber Bragg grating (SFBG); multimode fiber sensing; extreme environments; Hilbert transform; spectral demodulation; high-temperature measurement

Check for updates

Received: 29 September 2026
Revised: 29 October 2026
Accepted: 2 November 2026
Published: 4 November 2026

Copyright: © 2026 by the authors. Licensee MDPI, Basel, Switzerland. This article is an open access article distributed under the terms and conditions of the Creative Commons Attribution (CC BY) license.

1. Introduction

Accurate high-temperature measurement plays a critical role in advanced industrial fields, particularly in aerospace engineering and nuclear energy. In the aviation sector, the turbine inlet temperature of modern aero-engines frequently approaches or exceeds 1400 °C. Precise thermal monitoring is essential here to prevent structural overheating and stress

rupture. Similarly, operating temperatures in next-generation nuclear reactors have progressively increased. Very-high-temperature gas-cooled reactors now target operational ranges up to 1500 °C, requiring strict measurement accuracies to guarantee core safety [1–4]. Optical fiber sensors naturally suit these demanding environments due to their electromagnetic immunity and compact physical footprint. Existing research has extensively investigated the high-temperature applicability of silica fiber sensors through the use of engineered materials [5,6], specialized metal coatings, and thermal pre-annealing treatments [7]. However, constrained by the intrinsic thermal limits of silica, both conventional and engineered silica fiber Bragg gratings (FBGs) inevitably fail under ultra-extreme conditions. Beyond approximately 1000 °C, fused silica experiences irreversible refractive-index erasure and severe mechanical embrittlement [8,9]. Single-crystal sapphire fiber Bragg gratings (SFBGs) directly resolve this material bottleneck. Sapphire possesses a melting point exceeding 2040 °C and maintains strong chemical inertness. These physical properties enable SFBGs to operate stably in thermal regimes well beyond the limits of silica fibers, successfully demonstrating reliable sensing capabilities at temperatures reaching 1900 °C [10].

However, standard sapphire fibers lack a core-cladding structure due to current fabrication limitations. This unclad physical architecture inevitably supports highly multimode propagation. External environmental variations dynamically alter the excitation state and energy distribution among these numerous transverse modes. Such continuous modal instability severely compromises the fundamental measurement precision of the corresponding sensors. Overcoming this inherent limitation requires robust physical interventions that either stabilize the modal field or actively attenuate higher-order modes. Researchers have recently explored various structural modifications at the hardware level. Prominent physical strategies involve incorporating multimode lead-in fibers [11], introducing controlled bending geometries [12], employing chemical etching to reduce the waveguide diameter [13], constructing mode-field matched transitions [14–16], and directly developing true single-mode sapphire waveguides [17–20]. For instance, in 2009, Matthias Busch et al. utilized 50 m of multimode fiber (MMF) to comprehensively excite all guided modes, thereby obtaining a stable reflection spectrum [11]. Conversely, the majority of research has focused on suppressing higher-order modes to isolate the fundamental mode. In 2007, Zhan et al. achieved higher-order mode suppression by applying controlled bending to the sapphire fiber [12]. However, as the bending radius decreases, the attenuation of the fundamental mode increases simultaneously, causing significant difficulties in accurate peak detection. Subsequently, Yang et al. employed a hot acid etching technique to reduce the sapphire fiber diameter to 9 μm, successfully separating the modal reflection spectra [13]. Nevertheless, this aggressive chemical processing drastically compromised the intrinsic mechanical strength of the fiber. The milestone of realizing a quasi-single-mode (QSM) reflection spectrum in SFBGs was initially achieved in 2006 by Grobnic et al. through mechanical mode-field matching between a tapered single-mode fiber (SMF) and a sapphire fiber [14]. Advancing this concept, Bian et al. in 2024 utilized a fused biconical taper method to establish a robust connection between the SMF and sapphire fiber [15]. This structurally stable transition yielded a reliable QSM spectrum and enabled temperature measurements up to 1200 °C. Following this, Wu et al. employed femtosecond laser processing to inscribe a tapered waveguide within a coreless silica fiber [16]. This tailored mode-field matching interface also produced a QSM response, facilitating measurements up to 1600 °C. More recently, femtosecond laser micro-machining has driven the direct inscription of single-mode waveguide gratings within sapphire fibers. Researchers have successfully engineered various complex internal geometries. Prominent examples include depressed cladding waveguides [17,18], helical grating structures [19], and Bayesian neural network-optimized ring gratings [20]. These true single-mode architectures demonstrate stable thermal sensing

capabilities up to 1200 °C. However, the intricate fabrication processes severely restrict the inscription to relatively short waveguide lengths. Consequently, these internal structural modifications currently remain insufficient to satisfy the rigorous continuous monitoring demands across broad and extreme temperature profiles.

Given these fabrication bottlenecks, standard unclad multimode SFBGs continue to dominate practical high-temperature applications. The architecture remains the most mature option for extreme-environment monitoring [21–23]. Researchers typically secure stable read-outs using broad multimode excitation. This process involves adding long step-index silica lead-in fibers. Building on this robust hardware foundation, recent studies emphasize algorithmic demodulation. For instance, Eisermann et al. and Li et al. developed tracing techniques targeting the long-wavelength edge [24,25]. While highly effective under steady conditions, this edge-tracking mechanism exhibits sensitivity to extreme thermal environments. Intense high-temperature blackbody radiation can occasionally distort the local amplitude and shift the dynamic baseline. Similarly, Tan et al. proposed a multi-peak auto-tracking framework using cross-correlation algorithms [26]. This method performs excellently with stable reflection profiles. Under extreme thermal loads, however, the multimode envelope often undergoes continuous asymmetric distortion. This dynamic spectral variation can introduce matching uncertainties when relying on fixed reference templates. Other innovative approaches involve inscribing coincident gratings for multi-parameter discrimination [27]. This strategy utilizes sophisticated spatial laser machining. It represents an outstanding hardware-customized solution, leaving room for complementary algorithmic developments compatible with standard unclad sensors. Consequently, extracting reliable wavelengths from severely distorted multimode spectra remains a critical challenge. Deterministic demodulation strictly requires analyzing the macroscopic spectral envelope. This overall continuous profile accurately preserves the collective modal response despite localized degradation and dynamic noise. Such a macroscopic approach provides a robust and universal algorithmic pathway for unclad sensors.

This work establishes a deterministic demodulation framework based on spectral envelopes for multimode SFBG sensors. Traditional techniques frequently fail because they track unstable local sub-peaks or apply rigid empirical thresholds. The proposed strategy abandons these localized methods. It extracts the macroscopic resonant wavelength via a cascaded signal processing pipeline. Specifically, the framework integrates moving-average filtering, a Hilbert transform, and localized parabolic fitting. This mathematical sequence systematically suppresses high-frequency noise, defines the analytic envelope, and resolves the precise peak position. We validated this methodology using a single-crystal SFBG sensor from 23 °C to 1400 °C. The experimental data confirm that this envelope-oriented strategy effectively prevents algorithmic divergence and mitigates intense thermal background interference. It provides a reliable and computationally efficient interrogation solution for extreme high-temperature applications.

2. Principle

2.1. SFBG Fabrication and High-Temperature Sensing Configuration

The schematic configuration of the experimental setup for fabricating SFBGs via the line-by-line scanning method is depicted in Figure 1a. The system integrates a femtosecond (fs) laser inscription optical path, an in situ optical observation system, and an online reflection spectrum monitoring loop. In the laser fabrication path, a commercial fs laser (Pharos, Light-Conversion, Vilnius, Lithuania) emits pulses at a fundamental wavelength of 1030 nm with a temporal pulse duration of 290 fs and a repetition rate of 200 kHz. After frequency doubling through a second-harmonic crystal to yield a 515 nm output beam, the laser pulses pass sequentially through a variable attenuator, a half-wave polarization

rotator, and fixed beam apertures. The laser beam is directed by a dichroic mirror and tightly focused through a high-numerical-aperture oil-immersion objective (63×/NA = 1.40, Zeiss, Oberkochen, Germany) into the central region of a bare single-crystal sapphire fiber (Φ75, Micro Material Inc., Camarillo, CA, USA) immersed in index-matching oil (n = 1.51). The fiber is mounted on a high-precision computer-controlled XYZ motion stage (PlanarDL Two-Axis, ANT130LZS, Aerotech, Pittsburgh, PA, USA) to ensure sub-micrometer translation accuracy. A collinear Charge-Coupled Device (CCD) camera paired with an illumination source provides real-time microscopic imaging of the focal plane. Simultaneously, broadband light from a supercontinuum source (SuperK Compact, NKT Photonics, Birkerød, Denmark) is launched into the grating through an optical circulator and a 77 m lead-in MMF (62.5/125 μm, InfiniCor® 300, Corning, Corning, NY, USA), with the back-reflected spectrum captured in real time by an optical spectrum analyzer (OSA, AQ6370E, Yokogawa, Tokyo, Japan).

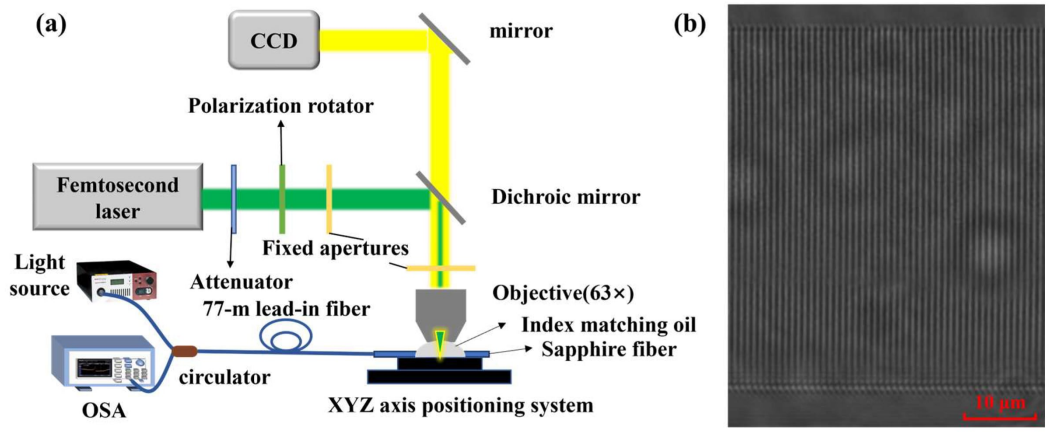


Figure 1. (**a**) The schematic diagram of the experimental setup for preparing an SFBG using a line-by-line scanning method. (**b**) A top-view microscope image of the finalized grating structure.

For grating inscription, optimized irradiation parameters were employed, including a single-pulse energy of 65 nJ and a stage translation velocity of 0.1 mm/s. According to the waveguide Bragg phase-matching condition [28]:

$$m\lambda_m = 2n_{\text{eff}}\Lambda \tag{1}$$

where n_{eff}, m denote the effective refractive index of the m-th mode, Λ is the grating period. And λ_m is the corresponding resonance wavelength. Here, we fabricated a second-order (m = 2) grating designed for a resonant wavelength of 1550 nm. The resulting grating pitch Λ was 0.8883 μm, and the total grating length was set to 2 mm. An optical microscope image displaying the microstructure of the fabricated SFBG is presented in Figure 1b, showing uniform inscribed lines with a width of approximately 50 μm.

Differentiating both sides of Equation (1) with respect to temperature T yields:

$$\frac{\mathrm{d}\lambda_{\text{B}}}{\mathrm{d}T} = \lambda_{\text{B}}\left(\frac{1}{n_{\text{eff}}}\frac{\partial n_{\text{eff}}}{\partial T} + \frac{1}{\Lambda}\frac{\partial \Lambda}{\partial T}\right) = \lambda_{\text{B}}(\xi_{\text{T}} + \alpha_{\text{T}}) \tag{2}$$

where $\xi_{\text{T}} = (1/n_{\text{eff}})(\partial n_{\text{eff}}/\partial T)$ and $\alpha_{\text{T}} = (1/\Lambda)(\partial\Lambda/\partial T)$ represent the thermo-optic coefficient and thermal expansion coefficient of single-crystal sapphire [8], respectively. Accordingly, the temperature sensitivity S_{T} is formulated as:

$$S_{\text{T}} = \frac{\mathrm{d}\lambda_{\text{B}}}{\mathrm{d}T} = \lambda_{\text{B}}(\xi_{\text{T}} + \alpha_{\text{T}}) \tag{3}$$

In sapphire crystals, the thermo-optic effect dominantly governs the positive spectral redshift. Because the unclad 75-μm sapphire fiber supports hundreds of high-order

transverse modes with distinct modal indices, thermal expansion and thermo-optic variations induce complex intermodal dispersion and non-uniform power redistribution across the broad modal spectrum. This severe spectral asymmetry and broadening at elevated temperatures necessitate the dedicated, robust envelope extraction algorithm developed below.

2.2. Demodulation Algorithm Architecture

As established from the multimodal phase-matching dynamics in Section 2.1, the lack of an optical cladding in the large-core single-crystal sapphire fiber allows dense transverse guided modes to propagate simultaneously with distinct effective indices. Consequently, the back-reflected spectrum manifests as a broad, highly asymmetric modal superposition spanning over 10 nm, characterized by steep trailing cut-off boundaries, extended rising tails, and intense intermodal interference ripples. When the sensor operates in extreme thermal regimes approaching 1400 °C, thermal blackbody radiation from the furnace chamber introduces substantial direct current (DC) baseline elevation, while elevated optoelectronic shot noise severely masks the underlying resonance. Conventional interrogation paradigms—such as single-peak Gaussian or Lorentzian nonlinear fitting and global centroid integration—are fundamentally built on the assumption of isolated, symmetric spectral responses. Under strong multi-mode skewness and variable radiation baselines, nonlinear fitting frequently suffers from local trap divergence and stochastic mode-hopping, whereas centroid integration undergoes persistent, massive systematic blue-shifts exceeding 15 nm. Moreover, simple empirical thresholding techniques fail to accommodate the extensive dynamic variation in optical power and background floor observed across broad thermal spans. To resolve these limitations deterministically without imposing unphysical symmetric profile assumptions or empirical intensity cuts, we introduce a spectrum-envelope-oriented, three-stage demodulation framework. The overarching computational architecture sequentially executes spectral denoising via optimized moving-average filtering, dynamic sub-band isolation through alternating current (AC)-domain Hilbert analytic envelope extraction, and continuous sub-pixel Bragg wavelength interrogation using a localized zero-centered parabolic operator. The detailed workflow of this hierarchical pipeline is illustrated in Figure 2. By systematically segregating high-frequency optoelectronic noise, macroscopic modal envelope boundaries, and the microscopic parabolic resonant crest, the framework converts a complex, ill-posed multimode peak-tracking problem into a sequence of closed-form, deterministic mathematical operations. In Stage 1, an optimized 201-point low-pass moving-average filter suppresses high-frequency detector shot noise and localized intermodal ripples while strictly safeguarding the steep modal cut-off edge against broadening distortion. In Stage 2, the filtered profile is projected into the linear power domain, where low-pass baseline subtraction isolates the high-temperature blackbody DC emission. The Cauchy principal value Hilbert transform is subsequently deployed on the AC modal fluctuations to construct a complex analytic signal, reconstructing the smooth macroscopic upper envelope. An adaptive 3 dB relative power criterion then self-consistently extracts the primary resonance sub-band $[\lambda_L, \lambda_R]$, effectively shielding subsequent operations from off-band thermal baselines and parasitic low-order modal humps. Finally, in Stage 3, within this gated sub-band, a derivative zero-crossing operator provides coarse localization of the physical crest, followed by a symmetric second-order parabolic fit across a narrow micro-window spanning ± 0.35 nm around the coarse apex. The continuous resonant wavelength λ_B is resolved analytically via vertex evaluation without iterative descent, entirely eliminating discrete spectrometer quantization steps and asymmetric pulling offsets. This complete architectural pipeline operates with closed-form $O(N)$ computational complexity, ensuring

both picometer-level interrogation fidelity and high-throughput real-time processing under extreme high-temperature environments.

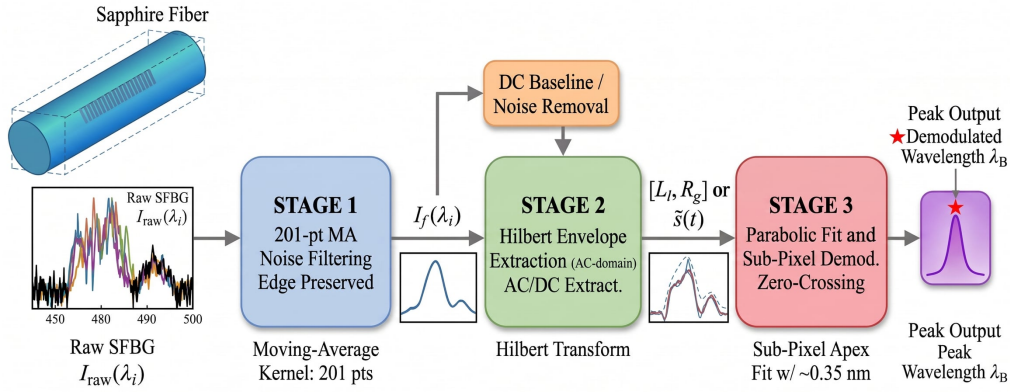


Figure 2. Flowchart of the proposed three-stage robust demodulation framework for multi-mode sapphire fiber Bragg gratings.

2.3. Spectral Noise Suppression via Moving Average Filtering

During high-temperature interrogation, the measured reflection spectrum is contaminated by high-frequency optoelectronic shot noise and fast-varying intermodal phase ripples. Let the raw digitized reflection spectrum be denoted as $I_{\mathrm{raw}}(\lambda_i)$, where $\lambda_i \in [\lambda_{\min}, \lambda_{\max}]$ represents the discrete sampling wavelength with an interrogation grid interval of $\Delta\lambda$. To eliminate spurious high-frequency noise spikes while preserving the underlying macroscopic envelope geometry, a symmetric moving-average low-pass filter is implemented:

$$I_{\mathrm{f}}(\lambda_i) = \frac{1}{2M+1} \sum_{k=-M}^{M} I_{\mathrm{raw}}(\lambda_{i+k}) \tag{4}$$

where $2M + 1$ designates the total filter window length. Symmetrical reflection boundary padding is enforced at both spectral edges to prevent edge attenuation and truncation artifacts. The selection of the window length $2M + 1$ represents a critical trade-off between high-frequency noise suppression and spectral peak fidelity, as experimentally evaluated in Figure 3. As shown in Figure 3a, the raw reflection spectrum contains dense high-frequency noise ripples superimposed on an intrinsically asymmetric envelope. When an insufficient window length such as $2M + 1 = 21$ points (21-pt) is deployed, as illustrated Figure 3b, residual high-frequency ripples persist across the crest region spanning from 1540 to 1550 nm, which can induce false local extremum locking. Conversely, an excessively wide window of $2M + 1 = 2001$ points in Figure 3d spans a spectral width comparable to the full-width at half-maximum (FWHM) of the SFBG reflection band. This oversmoothing averages the central resonance with the background floor, causing severe peak power depression exceeding 2.5 dB and completely flattening the steep trailing cut-off edge near 1550 nm into an unphysical profile. As demonstrated in Figure 3c, an optimized window of $2M + 1 = 201$ points is strategically deployed. Given the 0.05 nm sampling resolution of the optical spectrum analyzer, this 201-point window corresponds to a physical wavelength span of approximately 10 nm. This specific span is wide enough to effectively average out the dense intermodal ripples, yet remains significantly narrower than the macroscopic bandwidth of the SFBG reflection envelope. Consequently, it achieves the optimal balance, thoroughly eliminating high-frequency noise while rigorously preserving the authentic peak amplitude and steep modal boundary.

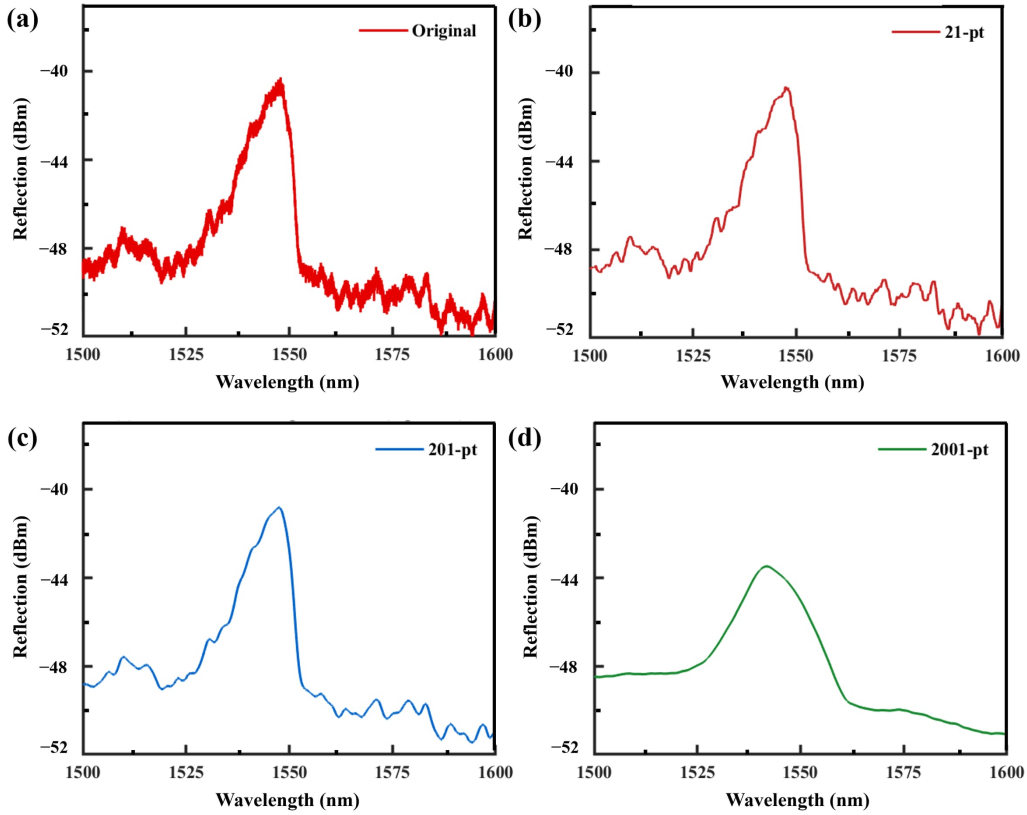


Figure 3. Reflection spectra of the unclad multimode SFBG under moving-average filtering with different window lengths $(2M + 1)$ at 23 °C: (**a**) raw spectrum, and filtered spectra with window lengths of (**b**) 21-pt, (**c**) 201-pt, and (**d**) 2001-pt.

2.4. Analytic Envelope Extraction and Adaptive Sub-Band Isolation

In ultra-high-temperature environments exceeding 800 °C, severe blackbody radiation emitted by the furnace tube superimposes a broad, temperature-dependent DC baseline onto the reflection spectrum, rendering static intensity thresholds unreliable. To dynamically isolate the dominant multimode reflection band without empirical thresholding, an analytic envelope extraction method based on the wavelength-domain Hilbert transform is implemented.

To avoid numerical distortion and phase inaccuracies caused by evaluating Cauchy principal value integrals over logarithmic data, the filtered spectrum $I_f(\lambda)$ is first converted into the linear power domain: $P_{lin}(\lambda) = 10^{I_f(\lambda)/10}$. A moving low-pass baseline $P_{base}(\lambda)$ is extracted to isolate the slowly varying DC thermal emission background, yielding the zero-mean fluctuating modal response $\Delta P(\lambda) = P_{lin}(\lambda) - P_{base}(\lambda)$. The discrete Hilbert transform $\tilde{P}_{ac}(\lambda)$ of this AC modal profile is formulated via the Cauchy principal value integral [29]:

$$\tilde{P}_{ac}(\lambda) = \mathcal{H}[\Delta P(\lambda)] = \frac{1}{\pi}\mathrm{P.V.}\int_{-\infty}^{+\infty} \frac{\Delta P(\tau)}{\lambda - \tau}\mathrm{d}\tau \tag{5}$$

Symmetric mirror extension is implemented prior to the transformation to eliminate finite-length boundary truncation errors. An analytic signal $Z(\lambda)$ in the spectral wavelength domain is subsequently synthesized:

$$Z(\lambda) = \Delta P(\lambda) + j\tilde{P}_{ac}(\lambda) \tag{6}$$

The macroscopic upper envelope $A_{\mathrm{lin}}(\lambda)$, characterizing the collective power distribution across the superimposed mode groups, is reconstructed by restoring the physical baseline onto the complex analytic modulus:

$$A_{\mathrm{lin}}(\lambda) = |Z(\lambda)| + P_{\mathrm{base}}(\lambda) = \sqrt{\Delta P^2(\lambda) + \tilde{P}^2_{\mathrm{ac}}(\lambda)} + P_{\mathrm{base}}(\lambda) \quad (7)$$

Upon converting back to the logarithmic scale, $A(\lambda) = 10\log_{10}[A_{\mathrm{lin}}(\lambda)]$, the analytic envelope smoothly circumscribes the global crest of the multimode reflection spectrum without undulating across minor modal beat ripples, as illustrated in Figure 4. Let $A_{\mathrm{max}} = \max\{A(\lambda)\}$ denote the global peak amplitude of the envelope. An adaptive 3 dB sub-spectral search window $[\lambda_{\mathrm{L}}, \lambda_{\mathrm{R}}]$ is self-consistently bounded at the relative half-power intersection points:

$$A(\lambda_{\mathrm{L}}) = A(\lambda_{\mathrm{R}}) = A_{\mathrm{max}} - 3\ \mathrm{dB} \quad (8)$$

where the precise boundary wavelengths λ_{L} and λ_{R} are resolved via localized two-point linear interpolation. As demonstrated in Figure 4, the dynamic sub-band is resolved with high geometric fidelity to $[\lambda_{\mathrm{L}}, \lambda_{\mathrm{R}}] = [1538.67\ \mathrm{nm}, 1550.87\ \mathrm{nm}]$, yielding an effective modal search bandwidth of $\Delta\lambda_{3\mathrm{dB}} = 12.20$ nm. This adaptive spatial gating strictly encloses the core multimode reflection energy while effectively rejecting low-order parasitic modal humps and high-temperature broadband background noise.

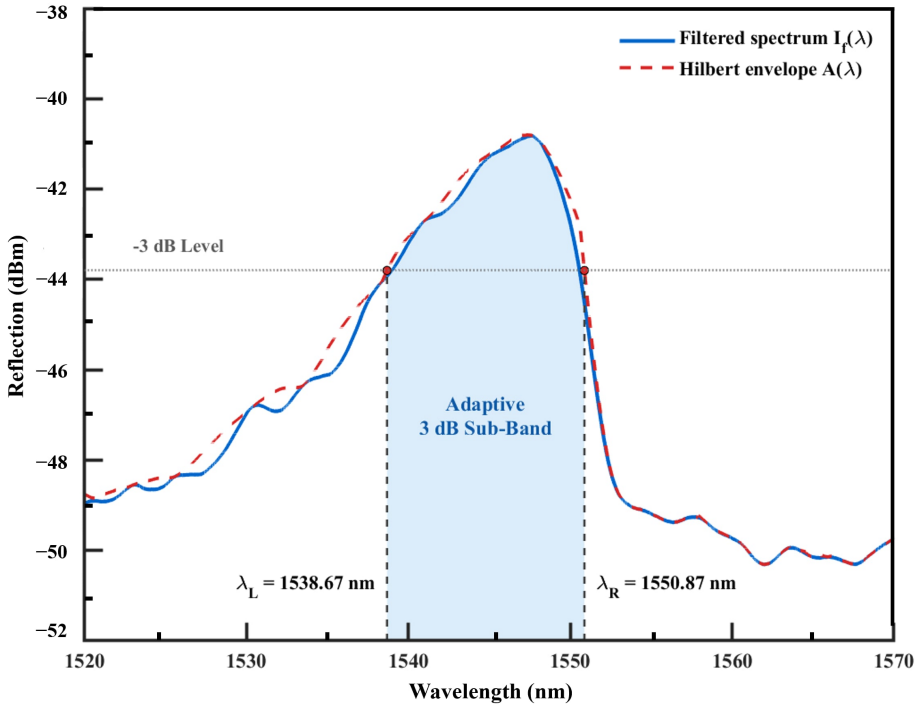


Figure 4. Analytic envelope extraction and adaptive 3 dB sub-band isolation based on the AC-domain Hilbert transform.

2.5. Localized Peak Identification

Once the dynamic sub-spectral window $[\lambda_{\mathrm{L}}, \lambda_{\mathrm{R}}]$ is adaptively isolated, the search space for the central Bragg wavelength is strictly confined to the primary modal resonance zone. However, directly locating the discrete maximum index via $\lambda_{\mathrm{raw}} = \mathrm{argmax}_{\lambda\in[\lambda_{\mathrm{L}}, \lambda_{\mathrm{R}}]}\{I_{\mathrm{f}}(\lambda)\}$ inherently restricts the measurement resolution to the physical sampling interval of the spectrometer, with $\Delta\lambda$ typically ranging from 0.02 to 0.05 nm. Furthermore, multi-mode modal competition occasionally flattens the crest profile, introducing discrete jumping artifacts during continuous thermal tracking.

To achieve continuous picometer-level tracking and eliminate discrete quantization errors without being distorted by the global spectral asymmetry, a localized derivative-assisted parabolic apex-fitting operator is implemented. The initial physical apex estimate $\lambda_{\text{peak}}^{(0)}$ is determined by locating the zero-crossing of the first-order numerical derivative:

$$\left.\frac{\mathrm{d}I_{\mathrm{f}}(\lambda)}{\mathrm{d}\lambda}\right|_{\lambda=\lambda_{\text{apex}}^{0}} = 0, \text{ with } \frac{\mathrm{d}^2 I_{\mathrm{f}}(\lambda)}{\mathrm{d}\lambda^2} < 0 \tag{9}$$

To eliminate the leftward pulling bias caused by the extended, gently sloping rising edge versus the steep trailing edge of the multimode spectrum, a strictly symmetric micro-neighborhood $\left[\lambda_{\text{apex}}^{(0)} - \Delta,\ \lambda_{\text{apex}}^{(0)} + \Delta\right]$ is extracted around the initial apex, where the empirically determined window $\Delta \approx 0.35$ nm is chosen to encompass only the immediate resonant tip. This specific value is optimized for the tested SFBGs to strictly balance the validity of the localized parabolic approximation against the algorithm's robustness to residual noise. Within this confined symmetric window, a second-order polynomial is fitted to the local spectral power:

$$I_{\text{fit}}(\lambda) = c_2\lambda^2 + c_1\lambda + c_0 \tag{10}$$

By analytically evaluating the extreme condition $\mathrm{d}I_{\text{fit}}/\mathrm{d}\lambda = 0$, the continuous demodulated Bragg wavelength λ_{B} is resolved uniquely at the parabola apex:

$$\lambda_{\mathrm{B}} = -\frac{c_1}{2c_2} \tag{11}$$

the condition $c_2 < 0$ guarantees a strictly downward local curvature, ensuring numerical stability and high determinism without iterative non-linear divergence. As depicted in Figure 5, this localized apex interrogation reliably converges to the true physical resonance center with a demodulation Bragg wavelength of 1547.612 nm at 23 °C. By isolating the micro-crest, this operator completely suppresses the quantization jump artifacts caused by the finite spectrometer sampling grid, avoids asymmetric pulling offsets, and enables smooth, picometer-level continuous wavelength tracking across extreme temperature variations up to 1400 °C.

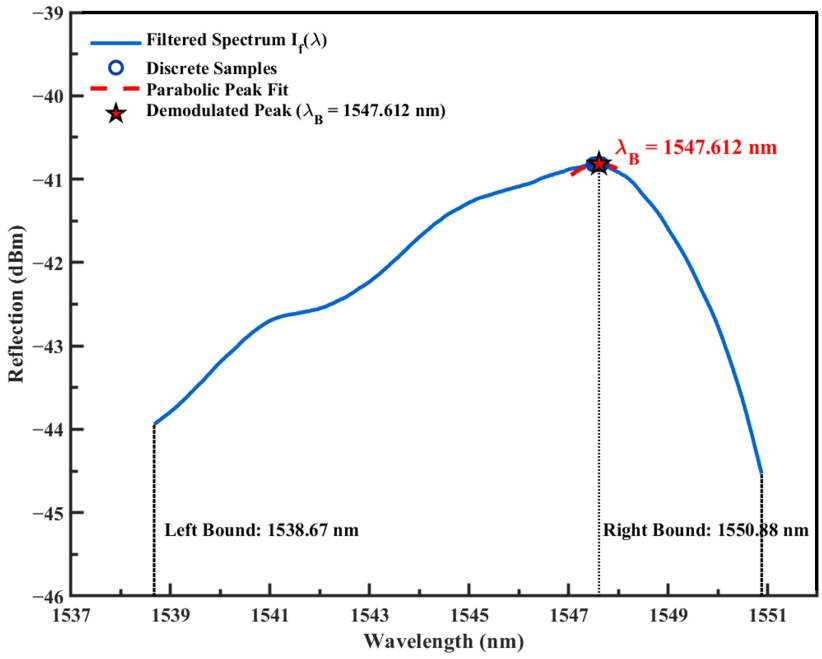


Figure 5. Continuous Bragg wavelength interrogation within the adaptively isolated sub-band based on localized parabolic peak fitting.

3. Result

3.1. High-Temperature Experimental Setup and Procedure

A dedicated high-temperature spectral interrogation and thermal calibration system was established to experimentally evaluate the tracking stability and accuracy of the proposed demodulation framework, as schematically illustrated in Figure 6. The optical interrogation path is configured in a reflection topology. The interrogation path is configured in a reflection topology. Broadband continuous light covering 450–2400 nm is emitted by the supercontinuum light source and delivered through the 2 × 1 MMF circulator into the fabricated SFBG sensor probe. The circulator simultaneously provides optical routing and back-reflection isolation to protect the light source. The SFBG sensor probe is installed inside the uniform hot zone of a high-temperature tubular resistance furnace. To eliminate mechanical vibration, air convection currents, and chemical contamination from the furnace hearth, the sensing region is loosely sleeved inside an open-ended high-purity alumina ceramic tube, ensuring unconstrained, stress-free thermal expansion.

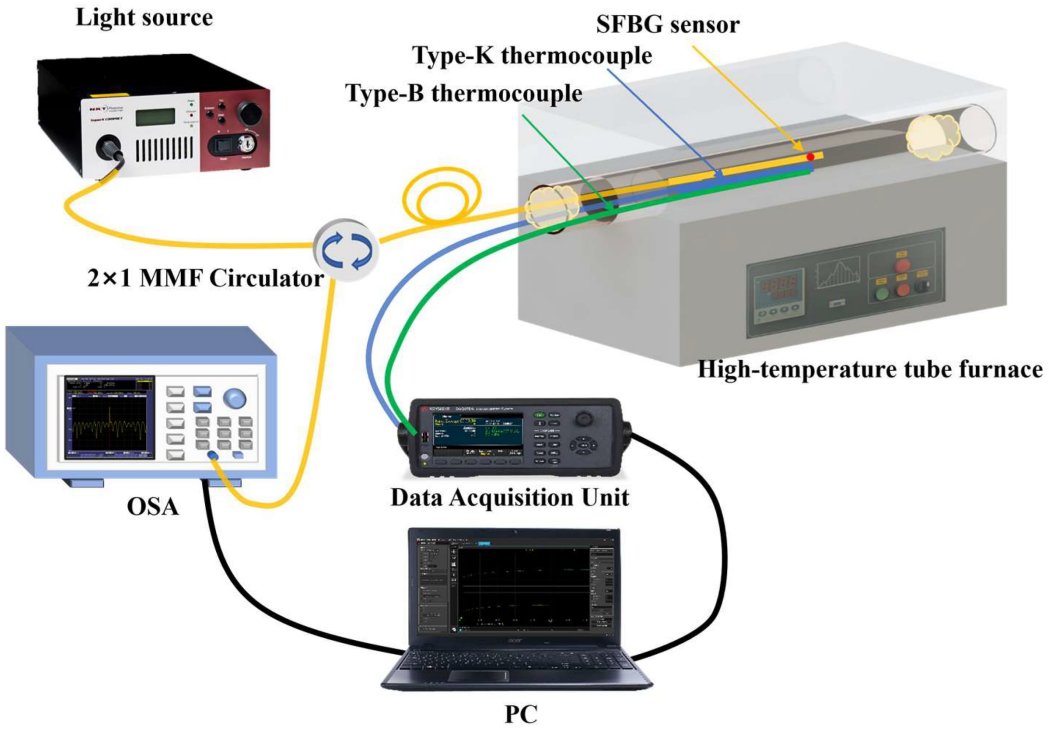


Figure 6. Schematic of the high-temperature sensing and testing experimental setup.

The multimode core resonance spectrum reflected by the SFBG travels back through the 2 × 1 MMF circulator and is captured by the OSA. To establish an accurate, cross-range temperature benchmark from room temperature to extreme heat, dual standard thermocouples—a Type-K thermocouple (optimized for high sensitivity in the low-to-medium range, 23–800 °C) and a platinum-rhodium Type-B thermocouple (dedicated to high stability in the extreme-temperature range, 800–1400 °C)—were positioned in close proximity to the SFBG tip. Both thermocouples are interfaced with a multi-channel data acquisition unit (Keysight Technologies, Santa Rosa, CA, USA) to record real-time thermal baselines. Spectral data from the OSA and synchronized thermal readings from the data acquisition unit are transmitted to a host personal computer (PC) for automated processing. The furnace temperature was stepped from 23 °C to 1400 °C. At each calibrated plateau, an isothermal dwell of 15 min was enforced to guarantee thermal equilibrium before spectral logging. The recorded spectra were subsequently processed by the proposed three-stage

demodulation framework to extract the continuous Bragg wavelength λ_B, enabling rigorous quantitative validation of the sensor's sensitivity, hysteresis, and noise immunity against the synchronized dual-thermocouple benchmark.

3.2. High-Temperature Testing and Discussion

The reflection spectra of the multimode SFBG sensor recorded across the calibrated temperature range of 23–1400 °C and the resulting thermal calibration characteristics are summarized in Figure 7. The raw reflection spectra undergo a continuous and pronounced red-shift from approximately 1547.6 nm to 1585.3 nm as the ambient temperature escalates, governed primarily by the positive thermo-optic coefficient and thermal expansion of single-crystal sapphire. However, exposure to extreme thermal environments inevitably induces multifaceted spectral degradation. When the temperature surpasses 800 °C and approaches 1400 °C, the background noise floor exhibits a noticeable elevation from approximately −51 dBm to −49 dBm due to thermal black-body radiation emitted from the furnace hearth, while inter-modal dispersion and differential modal attenuation trigger severe envelope flattening, asymmetric skewing toward the rising edge, and dense local modal splitting near the crest. These composite spectral perturbations substantially compress the effective signal-to-noise ratio and render traditional direct extremum readout or symmetric single-peak fitting schemes susceptible to random mode-hopping artifacts. To overcome these distortions, the raw spectra were processed sequentially via the proposed three-stage demodulation framework. The middle panel of Figure 7 illustrates the smoothed spectral profiles obtained after applying the optimized 201-point moving-average filter. High-frequency detector shot noise and fast-varying intermodal ripple interference are effectively filtered out, while the intrinsic multimodal profile and the steep trailing cut-off boundary are rigorously preserved without broadening distortion. Subsequently, the analytic envelope was extracted in the AC domain via the Hilbert transform to dynamically construct the self-adaptive 3 dB sub-band window, effectively shielding the interrogation process from off-band blackbody radiation baselines and remote modal ripples. Within this isolated 3 dB domain, localized derivative zero-crossing coupled with symmetric parabolic peak fitting was conducted. As demonstrated in the bottom panel of Figure 7, the extracted central Bragg resonance wavelengths λ_B, denoted by red star markers, deterministically lock onto the physical modal resonance center across all calibrated temperature setpoints including 23 °C, 200 °C, 404 °C, 605 °C, 805 °C, 1003 °C, 1200 °C, and 1400 °C. The continuous tracking trajectory progresses monotonically without false mode-hopping or quantization step errors across the entire 1400 °C test span.

The static thermal response and temperature testing characteristics of the SFBG sensor obtained during both heating-up cycles indicated by solid red squares and cooling-down cycles indicated by open blue circles are presented in Figure 8. As the temperature increases from 23 °C to 1400 °C, the demodulated central wavelength exhibits a pronounced non-linear red-shift, driven by the intrinsic temperature dependence of the thermo-optic coefficient ξ_T and thermal expansion coefficient α_T of single-crystal sapphire. By applying a second-order polynomial fitting to the heating calibration data, the relationship between the Bragg wavelength λ_B and temperature T is quantitatively expressed as:

$$\lambda_B(T) = 5.710 \times 10^{-6} T^2 + 2.017 \times 10^{-2} T + 1546.422 \quad (12)$$

with an exceptional determination coefficient of $R^2 = 0.9981$. Owing to this quadratic thermal behavior, the local temperature sensitivity increases monotonically with rising temperature, delivering values of 20.4 pm/°C at 23 °C, 27.0 pm/°C at 600 °C, and 36.2 pm/°C at 1400 °C. Moreover, the spectral peak positions recorded during the cooling-down cycle demonstrate exceptional congruence with the heating-up trajectory across all measured

temperature setpoints. The absence of discernible thermal hysteresis confirms both the high thermal durability of the femtosecond-laser-inscribed grating structure and the excellent measurement reproducibility of the proposed envelope extraction demodulation framework across full-range thermal cycles.

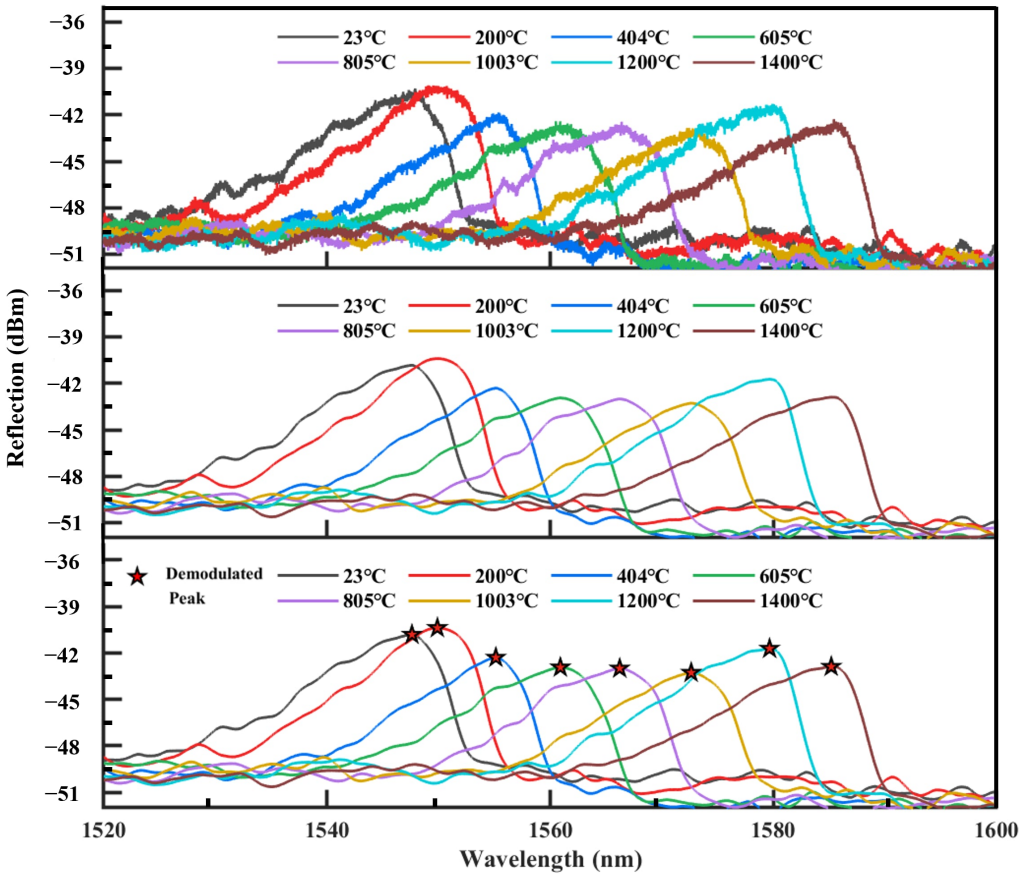


Figure 7. High-temperature sensing performance of the multimode SFBG from 23 °C to 1400 °C: Step-by-step demodulation spectral evolution: raw (**upper**), filtered (**middle**), and peak-tracked (**bottom**) spectra.

3.3. Multi-Temperature Isothermal Performance and Comparative Demodulation Analysis

To quantitatively evaluate the long-term tracking stability, noise immunity, and algorithmic robustness of the proposed framework under sustained extreme thermal environments, isothermal dwelling tests were performed across three characteristic temperature plateaus: 1000 °C, 1200 °C, and 1400 °C for a continuous duration of 60 min, as summarized in Figure 8. The demodulation performance of the proposed method was thoroughly benchmarked against three conventional techniques, including direct maximum detection (Direct Max), the traditional centroid algorithm (Centroid), and nonlinear Gaussian curve fitting algorithm (Gaussian). Figure 9a–c depict the temporal evolutions of the demodulated Bragg wavelengths obtained by the four algorithms during 60 min isothermal dwelling at 1000 °C, 1200 °C, and 1400 °C, respectively. Owing to intense intermodal interference, non-uniform baseline distortion induced by high-temperature blackbody radiation, and optoelectronic shot noise, the conventional algorithms exhibit severe systematic biases or pronounced high-frequency tracking fluctuations. Specifically, the centroid method displays a persistent systematic blue-shift of approximately 15–18 nm across all test plateaus, as exemplified by its stabilizing around 1566 nm at 1400 °C compared to the authentic reflection peak near 1585 nm. This substantial underestimation arises primarily from the broad asymmetric

reflection spectrum and broadband thermal radiation pulling the global energy integral toward shorter wavelengths. Similarly, the Gaussian fitting algorithm suffers from severe center misalignments, converging near 1546 nm across the testing window. When exposed to the extreme 1400 °C plateau shown in Figure 9c, the Gaussian fitting algorithm undergoes abrupt convergence failure and anomalous jumping at 50 min due to the flattened multi-peak profile, yielding an unacceptable standard deviation of $\sigma = 5.321$ nm. Meanwhile, although the Direct Max method tracks the vicinity of the actual resonance peak, it remains highly vulnerable to discrete spectral quantization and transient mode competition, leading to severe tracking jitter with standard deviations of $\sigma = 1.480$ nm at 1000 °C and $\sigma = 0.684$ nm at 1400 °C. In sharp contrast, the proposed method consistently delivers superior stability and high-fidelity peak localization throughout all three isothermal stages. By integrating moving-average filtering, AC Hilbert envelope 3 dB sub-band segmentation, and localized zero-centered parabolic peak extraction, the algorithm successfully shields the dominant resonance peak from non-uniform multi-mode distortions and elevated thermal radiation baselines. Figure 9d statistically benchmarks the standard deviations σ of the four algorithms at 1000 °C, 1200 °C, and 1400 °C. The proposed approach achieves remarkably tight standard deviations of $\sigma = 0.186$ nm at 1000 °C, $\sigma = 0.098$ nm at 1200 °C, and $\sigma = 0.158$ nm at 1400 °C. The slight elevation in σ at 1400 °C physically reflects the intensified thermal air convection inside the furnace tube and elevated photon noise, yet remains substantially lower than the jitter levels observed in the Direct Max and Centroid algorithms. These comparative results verify that the proposed demodulation framework possesses exceptional anti-noise robustness and measurement precision, ensuring reliable wavelength interrogation for ultra-high-temperature optical fiber sensing up to 1400 °C.

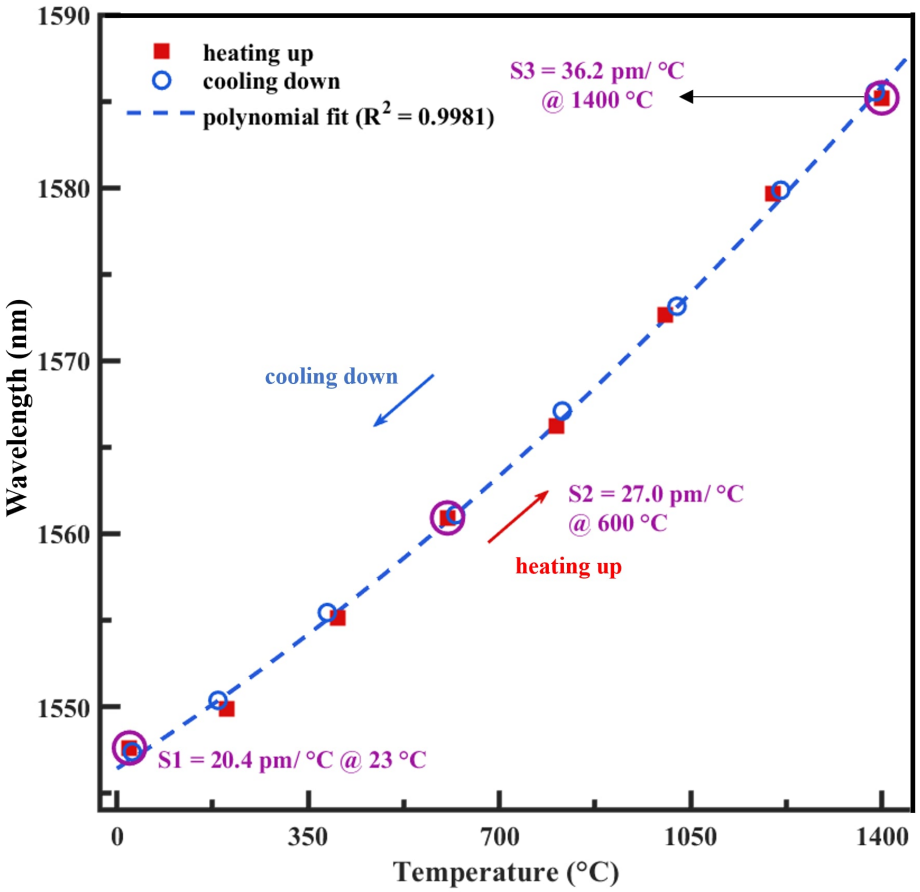


Figure 8. Bragg wavelength versus temperature during heating and cooling cycles with a second-order polynomial fit.

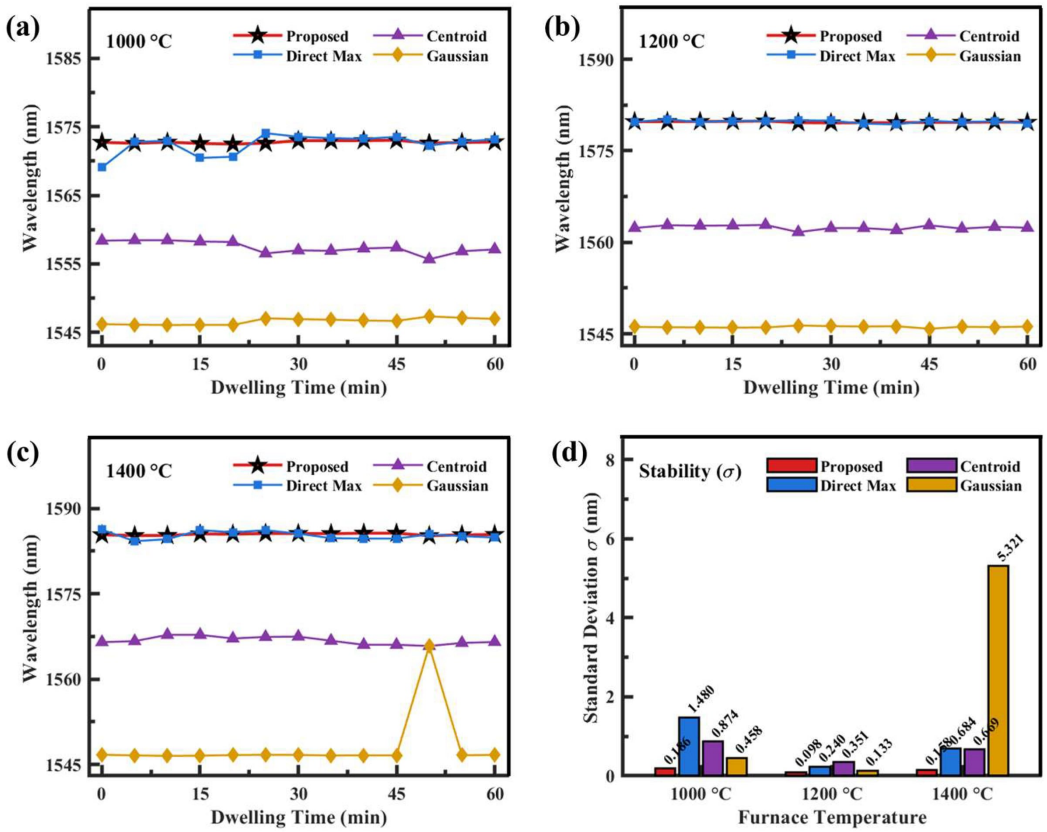


Figure 9. Isothermal stability and performance benchmarking of the four demodulation algorithms during continuous 60 min dwelling at different high-temperature plateaus: (**a**) 1000 °C; (**b**) 1200 °C; (**c**) 1400 °C; and (**d**) statistical comparison of wavelength standard deviations (σ) across the three dwelling temperatures.

4. Discussion

The experimental results and comparative benchmarks demonstrate that the proposed three-stage demodulation framework effectively overcomes the intrinsic physical limitations of multimode SFBGs in ultra-high-temperature environments. The primary challenge lies in a complex trade-off. We must eliminate broad spectral degradation—such as multimode skewness, intermodal phase ripples, and elevated thermal baselines—while strictly preserving the genuine Bragg resonance. The key to our superior performance is the hierarchical decoupling of noise, spectral boundaries, and apex localization. Conventional centroid integration is fundamentally prone to substantial short-wavelength blue-shifts of approximately 15 to 18 nm. This systematic error occurs due to wide spectral integration across asymmetrical tails and rising thermal emission. In contrast, our framework employs AC-domain Hilbert envelope extraction to establish an adaptive 3 dB sub-band. This mechanism self-consistently tracks the global energy crest. It intrinsically rejects low-order modal humps and DC background pedestals without relying on subjective empirical intensity thresholds. Furthermore, nonlinear curve-fitting methods like Gaussian or Lorentzian profiles suffer from algorithmic divergence and stochastic mode-hopping when the resonant peak flattens near 1400 °C. The localized zero-centered parabolic operator instead provides a deterministic closed-form solution. By isolating the physical micro-crest within a narrow, symmetric boundary spanning 0.35 nm, the framework effectively eliminates spectrometer quantization noise. It yields picometer-level wavelength tracking stability with standard deviations below 0.19 nm across all isothermal plateaus. From a computational perspective, the entire pipeline operates through non-iterative mathematical steps with an overall

complexity of $O(N)$. Empirical evaluations conducted on a standard personal computer (Intel Core i7, 16 GB RAM) via MATLAB R2019b demonstrate that the average execution time is approximately 15 ms per spectrum. Considering that the typical hardware sweep time of the optical spectrum analyzer takes approximately 4 s, this non-iterative mathematical pipeline introduces virtually zero processing delay. This renders the architecture highly suitable for deterministic, real-time signal demodulation in high-speed interrogation systems without imposing any computational bottlenecks. This completely avoids the heavy iterative descent loops typical of multi-peak nonlinear optimization, rendering the architecture highly suitable for deterministic, real-time signal demodulation in high-speed interrogation systems.

Table 1 presents a comprehensive performance comparison between our work and recently reported state-of-the-art SFBG demodulation methods [24–27]. While recent advancements report remarkably low measurement errors at extreme temperatures, these achievements predominantly rely on substantial hardware modifications or forced mode mixing. Spectral stabilization is frequently achieved by employing mechanical or electronic mode scramblers [24,27]. Other approaches append ultra-long multimode lead fibers that inevitably induce excessive transmission loss [25]. Furthermore, extreme low dispersion records often rely on rigid argon gas-sealed sapphire tubes. Such physical isolation completely fails if the rigid packaging is breached [26]. In sharp contrast, our proposed work deliberately targets the fundamental algorithmic challenge of standard unclad SFBGs. We directly confront the intensive thermal air convection and asymmetric blackbody radiation inherent in unconstrained 1400 °C environments, without utilizing physical mode scramblers or protective gas-sealed isolation. The unshielded exposure naturally captures a highly realistic physical fluctuation. Specifically, the standard deviation slightly increased to 0.158 nm at 1400 °C. This specific elevation indicates that severe thermal air convection inside the loosely sleeved tube furnace, combined with elevated photon shot noise, introduces residual high-frequency perturbations. Nevertheless, our algorithm effectively prevents mode-hopping and divergent errors. It proves exceptional universal algorithmic robustness for bare-fiber sensing.

Table 1. Performance comparison of representative SFBG sensors and demodulation methods for high-temperature measurement.

Reference	Sensor Architecture and Hardware Modifications	Method	Max Temp. and Reported Stability	Reported Performance at Extreme Temp.
Eisermann et al. [24]	Hybrid S-FBG; Requires mechanical mode-mixing	Edge tracking	1600 °C; ~10 K uncertainty	Accuracy severely degraded by mode variations; physical mode mixer is mandatory for stability.
Li et al. [25]	SFBG with added 500 m MMF	Wavelength detection	1380 °C; Residual < ±0.13 nm	Highly stable due to forced mode distribution, but excessive transmission loss prohibits low-reflectivity applications.
Tan et al. [26]	SFBG array; Argon gas-sealed in sapphire tube	Cross-correlation	1900 °C; Dispersion < ±12 pm	Extreme low dispersion achieved via gas-sealed thermal isolation; sensor fails entirely if rigid packaging breaks.

Table 1. *Cont.*

Reference	Sensor Architecture and Hardware Modifications	Method	Max Temp. and Reported Stability	Reported Performance at Extreme Temp.
Mumtaz et al. [27]	Coincident SFBGs; Requires electronic mode scrambler	Spatial discrimination	1600 °C; Calculated Error ~0.16 °C	Outstanding dual-parameter discrimination, but spectral stability explicitly relies on physical mode scrambling.
This work	SFBG with added 77 m MMF	Macroscopic envelope-fitting	1400 °C; $\sigma = 0.158$ nm (@1400 °C)	Universal algorithmic robustness; explicitly overcomes intensive air convection and blackbody radiation dynamically, without physical isolation.

5. Conclusions

This work reveals that envelope-based deterministic demodulation is well suited to resolve the intrinsic modal asymmetry and blackbody-noise-induced spectral degradation of multimode SFBGs under ultrahigh-temperature conditions. Instead of locking to fluctuating local sub-peaks, the proposed scheme identifies the macroscopic modal resonance center, thereby eliminating the root cause of random mode hopping and algorithmic divergence suffered by conventional Gaussian and centroid demodulation. The experimental results confirm that reliable wavelength tracking can be maintained up to 1400 °C, with negligible hysteresis over thermal cycling and robust stability during prolonged isothermal holds. By removing the requirement for fixed empirical thresholds, the method adapts spontaneously to time-varying spectral distortion and offers favorable computational efficiency. These features make the scheme attractive for high-temperature sensing scenarios where harsh thermal backgrounds distort the reflection profile.

Author Contributions: Conceptualization, Z.H. and C.X.; methodology, H.Z.; software, H.Z. and R.L.; validation, H.Z. and Q.Z.; formal analysis, H.Z. and Z.L. (Zhaoyi Li); investigation, H.Z. and E.W.; resources, Z.H. and C.X.; data curation, H.Z.; writing—original draft preparation, H.Z.; writing—review and editing, Z.H. and C.X.; visualization, H.Z. and Z.L. (Zhichun Liu); supervision, Z.H. and C.X.; project administration, Z.H.; funding acquisition, Z.H. and C.X. All authors have read and agreed to the published version of the manuscript.

Funding: This research received no external funding.

Institutional Review Board Statement: Not applicable.

Informed Consent Statement: Not applicable.

Data Availability Statement: The data supporting the findings of this study are available upon reasonable request to the corresponding author.

Conflicts of Interest: The authors declare no conflicts of interest.

References

1. Yaer, X.; Shimizu, K.; Qu, J.; Wen, B.; Cao, X.; Kusumoto, K. Surface deformation micromechanics of erosion damage at different angles and velocities for aero-engine hot-end components. *Wear* **2019**, *426–427*, 527–538. [CrossRef]
2. Burns, P.C.; Ewing, R.C.; Navrotsky, A. Nuclear fuel in a reactor accident. *Science* **2012**, *335*, 1184–1188. [CrossRef] [PubMed]
3. Lee, Y.; Lee, S.W.; Jo, H. Design and experimental analysis of heat-pipe-integrated heat exchanger for heat pipe nuclear microreactor. *Int. J. Energy Res.* **2025**, *2025*, 6681985. [CrossRef]
4. Chiesa, P.; Macchi, E. A thermodynamic analysis of different options to break 60% electric efficiency in combined cycle power plants. *J. Eng. Gas. Turbines Power* **2004**, *126*, 770–785. [CrossRef]
5. Cai, Y.; Yan, F.; Qin, Q.; Yang, D.; Feng, T.; Li, T.; Yu, C.; Wang, X.; Guo, H.; Ji, W.; et al. Thulium-doped fiber laser with wavelength switchable output and its utilization in temperature sensing. *Infrared Phys. Technol.* **2025**, *149*, 105923. [CrossRef]
6. Xian, F.; Lu, G.; Zheng, G. FBG-assisted no-core/hollow-core hybrid fiber for temperature and strain sensing. *IEEE Photonics Technol. Lett.* **2026**, *38*, 1379–1382. [CrossRef]
7. An, G.; Tao, Y.; Zhang, Z.; Jia, P. Annealing-improved gold-coated femtosecond fiber Bragg gratings for high-temperature sensing. *Photonics* **2026**, *13*, 509. [CrossRef]
8. Cavillon, M.; Lancry, M.; Poumellec, B.; Wang, Y.; Canning, J.; Cook, K.; Hawkins, T.; Dragic, P.; Ballato, J. Overview of high temperature fibre Bragg gratings and potential improvement using highly doped aluminosilicate glass optical fibres. *J. Phys. Photonics* **2019**, *1*, 042001. [CrossRef]
9. Mihailov, S.J. Fiber Bragg Grating Sensors for Harsh Environments. *Sensors* **2012**, *12*, 1898–1918. [CrossRef] [PubMed]
10. Habisreuther, T.; Elsmann, T.; Pan, Z.; Graf, A.; Willsch, R.; Schmidt, M.A. Sapphire fiber Bragg gratings for high temperature and dynamic temperature diagnostics. *Appl. Therm. Eng.* **2015**, *91*, 071201. [CrossRef]
11. Busch, M.; Ecke, W.; Latka, I.; Fischer, D.; Willsch, R.; Bartelt, H. Inscription and characterization of Bragg gratings in single-crystal sapphire optical fibres for high-temperature sensor applications. *Meas. Sci. Technol.* **2009**, *20*, 115301. [CrossRef]
12. Zhan, C.; Kim, J.H.; Lee, J.E.; Yin, S.; Ruffin, P.; Luo, C. High temperature sensing using higher-order-mode rejected sapphire-crystal fiber gratings. In *Photonic Fiber and Crystal Devices: Advances in Materials and Innovations in Device Applications*; Proc. SPIE 6698; SPIE: Bellingham, WA, USA, 2007; p. 66980F.
13. Yang, S.; Homa, D.; Pickrell, G.; Wang, A.B. Fiber Bragg grating fabricated in micro-single-crystal sapphire fiber. *Opt. Lett.* **2018**, *43*, 4268–4271. [CrossRef] [PubMed]
14. Grobnic, D.; Mihailov, S.J.; Ding, H.; Bilodeau, F.; Smelser, C.W. Single and low order mode interrogation of a multimode sapphire fibre Bragg grating sensor with tapered fibers. *Meas. Sci. Technol.* **2006**, *17*, 980–984. [CrossRef]
15. Bian, Q.; Zhu, H.T.; Liang, J.Q.; Yu, Y.; Yan, P.G. High-order mode suppression in sapphire fiber Bragg gratings based on mode field matching fusion splicing for single-mode demodulation systems. *IEEE Sens. J.* **2023**, *23*, 16953–16959. [CrossRef]
16. Wu, J.; Xu, X.; He, J.; Li, Z.; Bai, Z.; Weng, X.; Liu, L.; Qu, J.; Wang, Y.; He, J. Single-mode sapphire fiber Bragg grating high-temperature sensor. *Photonics Res.* **2025**, *13*, 3374–3382. [CrossRef]
17. Wang, M.; Salter, P.S.; Payne, F.P.; Liu, T.; Shipley, A.; Song, Z.; Morris, S.M.; Booth, M.J.; Fells, J.A.J. Optimization of single-mode sapphire waveguide Bragg gratings. *J. Lightwave Technol.* **2024**, *42*, 5629–5638. [CrossRef]
18. An, G.; Wang, Y.; Wang, H.; Liu, J.; Jia, P. Single-mode sapphire photonic crystal fiber Bragg grating. *Opt. Lett.* **2026**, *51*, 3269. [CrossRef] [PubMed]
19. Xu, X.; He, J.; Wu, J.; Chen, R.; Zhou, F.; Wang, B.; Zhang, Y.; Wang, Y.; He, J. Single-mode helical sapphire Bragg grating for high-temperature sensing. *J. Lightwave Technol.* **2025**, *43*, 2982–2987. [CrossRef]
20. He, C.; Wu, J.; Shu, X. Bayesian neural network-optimized single-mode sapphire ring Bragg grating for extreme high-temperature sensing. *Optica* **2026**, *13*, 1630–1642. [CrossRef]
21. Grobnic, D.; Mihailov, S.J.; Smelser, C.W.; Ding, H. Sapphire fiber Bragg grating sensor made using femtosecond laser radiation for ultrahigh temperature applications. *IEEE Photonics Technol. Lett.* **2004**, *16*, 2505–2507. [CrossRef]
22. Yang, S.; Hu, D.; Wang, A.B. Point-by-point fabrication and characterization of sapphire fiber Bragg gratings. *Opt. Lett.* **2017**, *42*, 4008–4011. [CrossRef] [PubMed]
23. Mumtaz, F.; Tekle, H.W.; Zhang, B.H.; Li, X.; Mathis, B.; Smith, J.D.; O'Malley, R.J.; Huang, J. Distributed Sapphire Fiber Bragg Grating-Based Thermal Profiling of Submerged Entry Nozzles. *IEEE Trans. Instrum. Meas.* **2025**, *74*, 9530112. [CrossRef]
24. Eisermann, R.; Krenek, S.; Habisreuther, T.; Ederer, P.; Simonsen, S.; Mathisen, H.; Elsmann, T.; Edler, F.; Schmid, D.; Lorenz, A.; et al. Metrological characterization of a high-temperature hybrid sensor using thermal radiation and calibrated sapphire fiber Bragg grating for process monitoring in harsh environments. *Sensors* **2022**, *22*, 1034. [CrossRef] [PubMed]
25. Li, Z.; Tan, Q.; Yan, Z.; He, J.; Du, B.; Xu, X.; Liu, S.; Liao, C.; Hu, Z.; Gao, L.; et al. Reliable wavelength detection method of sapphire fiber Bragg gratings using added multimode fiber. *Opt. Laser Technol.* **2025**, *182*, 112185. [CrossRef]
26. Tan, Q.; Li, Z.; Wu, J.; He, J.; Zhao, C.; Liao, C.; Wang, Y.; Xu, X.; He, J. Sapphire fiber Bragg gratings array demodulated with the multi-peak auto-tracking algorithm for quasi-distributed high-temperature measurement. *Opt. Express* **2025**, *33*, 414–423. [CrossRef] [PubMed]

27. Mumtaz, F.; Zhang, B.H.; Dey, K.; Smith, J.D.; O'Malley, R.J.; Huang, J. Discrimination of temperature and strain by characterizing two femtosecond laser-written coincident sapphire fiber Bragg gratings for harsh environment applications. *IEEE Trans. Instrum. Meas.* **2025**, *74*, 7004309. [CrossRef]
28. Kersey, A.D.; Davis, M.A.; Patrick, H.J.; LeBlanc, M.; Koo, K.P.; Askins, C.G.; Putnam, M.A.; Friebele, E.J. Fiber grating sensors. *J. Lightwave Technol.* **1997**, *15*, 1442–1463. [CrossRef]
29. Marple, S.L. Computing the discrete-time "analytic" signal via FFT. *IEEE Trans. Signal Process.* **1999**, *47*, 2600–2603. [CrossRef]

Disclaimer/Publisher's Note: The statements, opinions and data contained in all publications are solely those of the individual author(s) and contributor(s) and not of MDPI and/or the editor(s). MDPI and/or the editor(s) disclaim responsibility for any injury to people or property resulting from any ideas, methods, instructions or products referred to in the content.